

Denoising Weak Lensing Mass Maps with Deep Learning

Masato Shirasaki,^{1,*} Naoki Yoshida,^{2,3,4} and Shiro Ikeda^{5,6}

¹*National Astronomical Observatory of Japan (NAOJ), Mitaka, Tokyo 181-8588, Japan*

²*Department of Physics, University of Tokyo, Tokyo 113-0033, Japan*

³*Kavli Institute for the Physics and Mathematics of the Universe (WPI),*

University of Tokyo, Kashiwa, Chiba 277-8583, Japan

⁴*CREST, Japan Science and Technology Agency,*

4-1-8 Honcho, Kawaguchi, Saitama, 332-0012, Japan

⁵*Department of Statistical Science, School of Multidisciplinary Sciences,*

Graduate University for Advanced Studies, 10-3 Midori-cho, Tachikawa, Tokyo 190-8562, Japan

⁶*Graduate University for Advanced Studies, 10-3 Midori-cho, Tachikawa, Tokyo 190-8562, Japan*

(Dated: April 12, 2022)

Weak gravitational lensing is a powerful probe of the large-scale cosmic matter distribution. Wide-field galaxy surveys allow us to generate the so-called weak lensing maps, but actual observations suffer from noise due to imperfect measurement of galaxy shape distortions and to the limited number density of the source galaxies. In this paper, we explore a deep-learning approach to reduce the noise. We develop an image-to-image translation method with conditional adversarial networks (CANs), which learn efficient mapping from an input noisy weak lensing map to the underlying noise field. We train the CANs using 30000 image pairs obtained from 1000 ray-tracing simulations of weak gravitational lensing. We show that the trained CANs reproduce the true one-point probability distribution function of the noiseless lensing map with a bias less than 1σ on average, where σ is the statistical error. Since a number of model parameters are used in our CANs, our method has additional error budgets when reconstructing the summary statistics of weak lensing maps. The typical amplitude of such reconstruction error is found to be of $1 - 2\sigma$ level. Interestingly, pixel-by-pixel denoising for under-dense regions is less biased than denoising over-dense regions. Our deep-learning approach is complementary to existing analysis methods which focus on clustering properties and peak statistics of weak lensing maps.

I. INTRODUCTION

Gravitational lensing is a relativistic effect that causes characteristic distortion of the images of distant astrophysical sources. The degree of distortion is determined by the gravitational potential of intervening mass (lens) and the geometry between the lens and source objects [1]. Although the induced distortion is tiny for individual sources, averaging over a large number of sources can reveal the gravitational lensing effect due to large-scale mass distribution in the Universe. In the literature, the lensing effect caused by the large-scale structure is referred to as weak lensing effect. The great advantage of measuring the weak lensing effect is that it enables us to study the matter density distribution in a physical and unbiased manner in principle. Statistical analysis of weak lensing effect is one of the most important studies in modern cosmology; one can extract rich information of gravitational clumping of dark matter and cosmic expansion (see, Refs [2–4] for reviews).

The two-point angular correlation function of shapes of sources, or its Fourier-space counterpart known as power spectrum, are commonly used to characterize weak lensing maps. Although the power spectrum provides a complete statistical description of a random Gaussian field, numerical simulations of weak lensing effect have shown

that weak lensing maps have non-Gaussian properties. Hence the power spectrum alone cannot fully describe a weak lensing map [5–7]. Various statistical methods have been proposed to study the non-Gaussian features [8–19]. Most of these proposed methods consider two-dimensional maps, i.e., images.

Distortion of galaxy shape is commonly used as a measure of weak lensing effect. The weak lensing effect of individual galaxies is expected to be much smaller than the intrinsic shape in practice [4], and the shape measurement is affected by various observational effects [20], rendering the measurement and the resulting statistics uncertain. These are altogether called "shape noises", which make weak lensing maps estimated from galaxy shape to be intrinsically noisy. Often the original cosmological information imprinted in the map is obscured. There exist several approaches to reduce the shape noise in weak lensing maps in the literature [21–26], but it is still challenging to obtain a completely noiseless weak lensing map from observations with an angular resolution of ~ 1 arcmin.

In this paper, we examine a deep-learning approach to generate a high-resolution weak lensing map from noisy, observed one. The procedure is essentially an image-to-image translation from a noisy input map to the underlying noise field. We adopt the conditional adversarial networks for image-to-image translation used in Ref. [27]. We train and validate the networks by using 30000 noisy weak lensing maps based on cosmological weak lensing simulations. The training is performed with effective an-

* masato.shirasaki@nao.ac.jp

gular resolution of ~ 1.5 arcmin, and we assume that the root-mean-square error of the input noisy maps is totally dominated by the shape noise. We then test the trained networks by using additional 1000 data sets and investigate if our deep-learning method can reproduce two summary statistics of weak lensing maps in absence of noise: one is the power spectrum and the other is one-point probability distribution function (PDF). We also aim at reconstruction of noise-free weak lensing map on pixel-by-pixel basis.

The paper is organized as follows. In Section II, we summarize the basics of gravitational lensing. In Section III, we describe the conditional adversarial networks adopted in this paper and provide how to produce the data set for training, validating, and testing the networks. In Section IV, we show the performance of our trained networks when applying them to test data set. Future prospects in upcoming surveys with higher source number density are discussed in Section V. Concluding remarks and discussions are given in Section VI.

II. WEAK GRAVITATIONAL LENSING

A. Basics

Weak lensing effect is commonly characterized by the distortion of image of a source object (galaxy) by the following 2×2 matrix between the observed position of a source object $\boldsymbol{\theta}_{\text{obs}}$ and the true (unlensed) position $\boldsymbol{\theta}_{\text{true}}$:

$$A_{ij} = \frac{\partial \theta_{\text{true}}^i}{\partial \theta_{\text{obs}}^j} \equiv \begin{pmatrix} 1 - \kappa - \gamma_1 & -\gamma_2 - \omega \\ -\gamma_2 + \omega & 1 - \kappa + \gamma_1 \end{pmatrix}, \quad (1)$$

where κ is the convergence, γ is the shear, and ω is the rotation. In the weak lensing regime ($\kappa, \gamma \ll 1$), the convergence can be expressed as the integral of the density contrast of underlying matter density field $\delta_{\text{m}}(\boldsymbol{x})$ with a weight over redshift [1],

$$\kappa(\boldsymbol{\theta}) = \int_0^\infty d\chi W_\kappa(\chi) \delta_{\text{m}}(r(\chi)\boldsymbol{\theta}, \chi), \quad (2)$$

$$W_\kappa(\chi) = \frac{3}{2} \left(\frac{H_0}{c} \right)^2 \Omega_{\text{m}0} (1 + z(\chi)) r(\chi) \times \int_\chi^\infty d\chi' p(\chi') \frac{r(\chi' - \chi)}{r(\chi')}, \quad (3)$$

where H_0 is the present-day Hubble constant, $\Omega_{\text{m}0}$ is the matter density parameter at present, $\chi(z)$ is the radial comoving distance to redshift z , $r(\chi)$ is the angular diameter distance, and $p(\chi)$ represents the source distribution normalized to $\int d\chi p(\chi) = 1$. Throughout this paper, we assume that the source galaxies are located at a single plane at redshift of $z_{\text{source}} = 1$, i.e. $p(\chi) = \delta(\chi - \chi_1)$ where $\delta(x)$ is the Dirac delta function and $\chi_1 = \chi(z = 1)$ for simplicity.

B. Estimator of convergence field

The lensing convergence κ is of our primary interest since it contains rich cosmological information. In the following, we summarize how to estimate κ from observables in modern galaxy imaging surveys. We first define the smoothed convergence map (field) as

$$\hat{\kappa}(\boldsymbol{\theta}) = \int d^2\phi \kappa(\boldsymbol{\theta} - \boldsymbol{\phi}) U(\boldsymbol{\phi}), \quad (4)$$

where U is the filter function to be specified below. We can calculate the same quantity by smoothing the shear field γ as

$$\hat{\kappa}(\boldsymbol{\theta}) = \int d^2\phi \gamma_+(\boldsymbol{\phi} : \boldsymbol{\theta}) Q_+(\boldsymbol{\phi}), \quad (5)$$

where γ_+ is the tangential component of the shear at position $\boldsymbol{\phi}$ relative to the point $\boldsymbol{\theta}$. The filter function for the shear field Q_+ is related to U by

$$Q_+(\boldsymbol{\theta}) = \int_0^{\theta_o} d\theta' \theta' U(\theta') - U(\boldsymbol{\theta}). \quad (6)$$

We consider a filter function Q_+ that has a finite extent. In such cases, one can write

$$U(\boldsymbol{\theta}) = 2 \int_\theta^{\theta_o} d\theta' \frac{Q_+(\boldsymbol{\theta}')}{\theta'} - Q_+(\boldsymbol{\theta}), \quad (7)$$

where θ_o is the outer boundary of the filter function. Note that the filter function U should be compensated because the smoothed field $\hat{\kappa}$ does not depend on undetermined constant [28].

In this paper, we consider the truncated Gaussian filter (for U):

$$U(\boldsymbol{\theta}) = \frac{1}{\pi\theta_G^2} \exp\left(-\frac{\theta^2}{\theta_G^2}\right) - \frac{1}{\pi\theta_o^2} \left[1 - \exp\left(-\frac{\theta_o^2}{\theta_G^2}\right) \right], \quad (8)$$

$$Q_+(\boldsymbol{\theta}) = \frac{1}{\pi\theta^2} \left[1 - \left(1 + \frac{\theta^2}{\theta_G^2} \right) \exp\left(-\frac{\theta^2}{\theta_G^2}\right) \right], \quad (9)$$

for $\theta \leq \theta_o$ and $U = Q_+ = 0$ elsewhere. Throughout this paper, we set $\theta_o = 30$ arcmin and $\theta_G = 1.5$ arcmin. The choice of $\theta_G = 1.5$ arcmin is found to be an optimal smoothing scale for the detection of massive galaxy clusters using weak lensing for $z_{\text{source}} \sim 1$ [29].

In actual observations, ellipticity of galaxies is used as an indicator of the shear field. The observed ellipticity of galaxy can be decomposed into two parts as

$$\epsilon_{\text{obs}} = \epsilon_{\text{N}} + \gamma, \quad (10)$$

where ϵ_{obs} and ϵ_{N} are the observed ellipticity and shape noise, respectively. In typical galaxy imaging surveys, the shape noise term is mostly contributed by the intrinsic ellipticity of source galaxies and the shape measurement inaccuracy. Since we expect both are independent

of weak lensing shear γ , the smoothed convergence estimated by Eq. (5) can be expressed as

$$\kappa_{\text{obs}} = \kappa_{\text{N}} + \kappa, \quad (11)$$

where the left-hand side represents the observed convergence, while κ_{N} in the right-hand side is the noise convergence from the shape noise. The primary purpose of this paper is to estimate the underlying convergence field κ from the observed map κ_{obs} . To this end, we adopt an image-to-image translation based on conditional adversarial networks.

III. METHOD

A. Image-to-Image Translation

We use conditional adversarial networks developed in Ref [27], referred to as `pix2pix`, for denoising the weak lensing convergence field. `pix2pix` is designed so as to learn mapping from input to output, but also to learn a loss function associated with this mapping. Therefore, it provides a generic approach to image-to-image translation problems, and is free from the formulation of loss function in the networks on a problem-by-problem basis.

The networks have two main pieces, a generator and a discriminator. The generator applies some transform to the input image to get an output image. The discriminator compares the input image to an unknown image (either a target image from the data set or an output image from the generator) and tries to guess if it is produced by the generator.

The generator in `pix2pix` uses a U-Net which is a kind of encoder-decoder structure [30]. On the encoder part in the generator, an input image is progressively compressed with eight convolution layers. In this compression process, the generator tries to learn the important features of the input at different scales. Each convolution layer consists of convolution with a kernel size of 5×5 , the batch normalization, and the application of activation function of leaky ReLU with a leak slope of 0.2. When arriving at the final convolution layer, the generator performs the inverse operation of convolution layer and combines the simplified feature from the final convolution layer into more and more complicated representations. In addition, the U-Net has additional skip connections between mirrored layers in the encoder and decoder stacks, allowing to propagate the small-scale information that would be lost as the size of the images decreases in the encoder.

In the discriminator, a given set of target and input images are reduced with 4 convolution layers and then all responses are averaged out to provide the ultimate output. The final output in the discriminator is used to determine if the input is real or fake.

In this paper, we adopt the structure of the generator and the discriminator as shown in Figure 1. To obtain underlying convergence from an input noisy map, we first

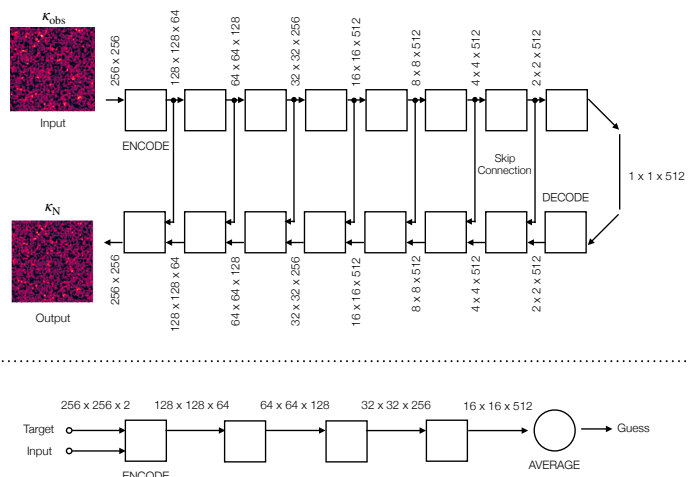


FIG. 1. The structure of conditional adversarial networks in this paper. The upper portion represents the generator that tries to translate an input noisy weak lensing map κ_{obs} to the underlying noise field κ_{N} . The lower shows the discriminator which guesses if the input image has been produced by the generator or not. Both of the generator and discriminator consist of a series of (de)convolution layers and the resulting number of model parameters in the networks is close to 4 millions.

perform an image-to-image translation from a noisy lensing map κ_{obs} to the underlying noise field κ_{N} ¹. Once the noise field is predicted by the networks, we then estimate the underlying convergence κ by subtracting the predicted noise from the observed map κ_{obs} .

B. Ray-tracing simulation

To construct a large data set for deep learning, we utilize ray-tracing simulations of gravitational lensing in Ref [31]. The simulations are based on 200 realizations of high-resolution N -body simulations with a box size of $240 h^{-1}$ Mpc on a side. The N -body simulations are performed with the number of particles of 256^3 for the concordance Λ CDM model². We work with a single source redshift at $z_{\text{source}} = 1$. The ray-tracing simulations are

¹ In Appendix A, we also examine the training so that the generator can predict the underlying noiseless convergence field from noisy input, but such training is found to be less effective for denoising.

² The following cosmological parameters are adopted in the simulations: the matter density $\Omega_{\text{m}0} = 0.238$, the baryon density $\Omega_{\text{b}} = 0.042$, the dark energy density $\Omega_{\Lambda} = 1 - \Omega_{\text{m}0} = 0.762$, the equation of state parameters of dark energy $w = -1$, the scalar spectral index $n_{\text{s}} = 0.958$, the amplitude of curvature perturbations $A_{\text{s}} = 2.35 \times 10^{-9}$ at $k = 0.002 \text{ Mpc}^{-1}$, Hubble parameter $h = 0.732$, and the variance of the present-day density fluctuation in a sphere of radius $8 h^{-1}$ Mpc $\sigma_8 = 0.76$.

performed on 2048^2 pixels with the pixel size of 0.15 arcmin. From the 200 N -body simulations, they have produced 1000 realizations of 5×5 squared-degrees lensing fields by rotating and shifting the structures in N -body simulations randomly. Details of the ray-tracing simulations are found in Ref [31].

When producing a training set for deep learning, we first degrade the lensing shear fields on 512^2 pixels by averaging over nearby 4 by 4 pixels (the degraded pixel size is then 0.6 arcmin). We then randomly subtract the contiguous area consisting of 256^2 pixels to increase the number of training sets. We perform the random subtraction 100 times for individual simulations with 512^2 pixels. For the main training data set, we use 600 realizations of lensing shear among 1000 parent realizations, and then have 60000 shear fields with a total sky coverage of 2.5×2.5 squared degrees. We also produce another 1000 shear fields for testing the networks from remaining 10 realizations. To create a noisy field, we include galaxy shape noise ϵ_N in our simulation by adding to random ellipticities which follow the two-dimensional Gaussian distribution as

$$P(\epsilon_N) = \frac{1}{\pi\sigma_N^2} \exp\left(-\frac{\epsilon_N^2}{\sigma_N^2}\right), \quad (12)$$

where $\epsilon_N = \sqrt{\epsilon_{N,1}^2 + \epsilon_{N,2}^2}$ and $\sigma_N^2 = \sigma_\epsilon^2 / (n_{\text{gal}} \theta_{\text{pix}}^2)$ with the pixel size of $\theta_{\text{pix}} = 0.6$ arcmin. In this paper, we set $\sigma_\epsilon = 0.35$ and $n_{\text{gal}} = 20 \text{ arcmin}^{-2}$. These correspond to the typical value of the current-generation ground-based imaging survey [32]. We prepare 60000 and 1000 realizations of the random ellipticities for training and testing, respectively.

C. Setup of Training and Validation

The objective of our networks is expressed as

$$\arg \min_G \max_D \left\{ \mathcal{L}_{\text{cGAN}}(G, D) + \lambda \mathcal{L}_{\text{L1}} \right\}, \quad (13)$$

where G is the generator and D is the discriminator. We here introduce two loss functions as

$$\mathcal{L}_{\text{cGAN}}(G, D) = \mathbb{E}_{x,y} \log D(x, y) + \mathbb{E}_{x,z} \log \{1 - D(x, G(x, z))\}, \quad (14)$$

$$\mathcal{L}_{\text{L1}}(G) = \mathbb{E}_{x,y,z} \sum_{\text{map}} |y - G(x, z)|, \quad (15)$$

where x is the input vector, y is the output vector, and z is a random noise vector at the bottom layer of the generator. In Eq. (15), the summation runs over all the pixels in a map. In the training, we alternate between one gradient descent step on D , then one step on G . As suggested in Ref. [33], we train to maximize the term of $\log D(x, G(x, z))$. In addition, we divide the objective by 2 while optimizing D , which slows down the learning rate of D relative to G .

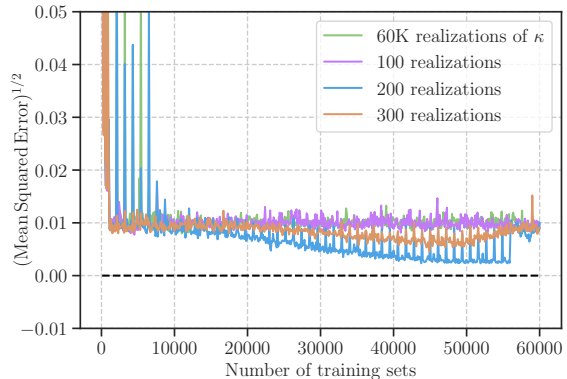


FIG. 2. The mean squared error of the lensing convergence maps in the training process. We measure the mean squared error of the validation data set at different epochs in training. In this figure, the colored lines show the training processes based on different realizations of the true convergence: *Green*: the number of realization of true maps is 60000. *Purple*: Among 60000 realizations (green), we select 100 realizations before training. *Blue*: Similar to purple one, but we select 200 realizations. *Orange*: Similar to purple one, but we select 300 realizations. This figure shows that $\simeq 200$ realizations of noiseless convergence is suitable to learn the image-to-image translation in an efficient way.

When training the networks, we use the minibatch Stochastic Gradient Descent (SGD) method and apply the Adam solver [34], with learning rate 0.0002, momentum parameters $\beta_1 = 0.5$ and $\beta_2 = 0.9999$. We also set $\lambda = 100$ in Eq. (13). All the networks in this paper are trained with a batch size of 1. We initialize the model parameters in the networks from a Gaussian distribution with mean 0 and standard deviation 0.02. We train our networks using the TensorFlow implementation³ of `pix2pix` on a single NVIDIA Quadro P5000 GPU. While processing, we randomly select training and validation data from the input data sets. Each network is validated every time it learns 100 image pairs. The training procedure takes 0.5 – 2 seconds per an image pair, and about a few hours for learning 10000 image pairs.

Producing a realization of noisy data set κ_{obs} is non-trivial for our training task, because we use two different independent realizations of the noise κ_N and lensing field of interest, κ . To optimize the training, we test four cases as:

1. The input data set consists of 60000 independent realizations of κ_N . When adding the lensing convergence κ to produce a noisy data, we use different realizations of κ from 60000 different realizations.

³ <https://github.com/yenchenlin/pix2pix-tensorflow>

2. Similar to case 1, but we restrict the number of realization of κ to be 300. When adding κ to the noise κ_N , we choose the map from 300 realizations at random.
3. Similar to case 2, but we use the number of realization of κ to be 200.
4. Similar to case 3, but we use the number of realization of κ to be 100.

In Case 1, we train the networks using 60000 independent noisy maps. We expect that there is some optimal number of realizations of κ in the training process, since too many realizations will make an efficient learning difficult for the networks, while fewer realizations can not provide a sufficient information for the image-to-image translation. From this point of view, Case 1 corresponds to oversampling of κ for training.

To find the optimal number of realizations of κ , we measure the mean squared error (MSE) in image space for validation sets. Figure 2 shows the MSEs for four different input data sets as a function of the number of training sets. Clearly, efficient learning of image-to-image translation is achieved when we use ~ 200 realizations of κ to produce noisy data set. In the following, we use 200 realizations to produce noisy data for training. The predicted noise images by the generator with $\gtrsim 40000$ training sets show unrealistic fluctuations between nearby pixels, while the predicted noise images are smooth enough if the network uses 20000 – 40000 training sets.

In general, the optimal number of training sets depends on a number of factors. For our purpose of cosmology study here, it is important to train so that the estimation of summary statistics is unbiased. Hence, we try to find the optimal number by using two common summary statistics in cosmological studies. One is power spectrum defined as

$$\langle \tilde{\kappa}(\ell_1) \tilde{\kappa}(\ell_2) \rangle \equiv (2\pi)^2 \delta^{(2)}(\ell_1 - \ell_2) C_\kappa(\ell_1), \quad (16)$$

where $\tilde{\kappa}$ is the Fourier transform of a noiseless convergence field, $\delta^{(n)}(\mathbf{x})$ is the Delta function in n -dimensional space, and $C_\kappa(\ell_1)$ is the power spectrum. The other statistic is the one-point probability distribution function (PDF) \mathcal{P} of lensing convergence in real space. Note that the power spectrum is a measure of Gaussian information in κ fields, while the PDF can capture some non-Gaussian information such as skewness and kurtosis.

We examine three cases with 20000, 30000, and 40000 sets when training our networks. After training, we input the test data set to the generator, in order to have lensing convergence predictions by the networks, denoted as κ_{DL} . We use 1000 independent realizations of noisy lensing convergence for testing the network. Note that the data set in testing process is independent of the ones used in training. We then measure the power spectrum and the PDF of κ_{DL} . We also measure them for the corresponding true map κ_{true} . We normalize the lensing convergence so as to have a zero mean and a unit

variance. This normalization is necessary to discern a small difference of summary statistics between κ_{DL} and κ_{true} . We employ 20 bins logarithmically spaced in the range of $\ell = 100$ to 10^5 when measuring the power spectra. We measure the PDF in 100 linear spaced bins in the range of $(\kappa - \mu)/\sigma = [-5, 15]$, where μ is the mean and σ is the standard deviation of lensing convergence over a sky coverage of 2.5×2.5 squared degrees. Comparing the summary statistics of the predicted and true convergence fields, we will find how many realizations of input data sets are required to minimize the difference of statistics. Furthermore, we study the dependence of model prediction by the networks on different realizations of training sets by constructing 10 bootstrap subsamples of 20000 – 40000 realizations from parent 60000 realizations.

IV. RESULTS

In this section, we summarize the performance of denoising weak lensing maps by our deep-learning approach.

A. Visual impression

We first show a visual comparison among three lensing fields, an input noisy convergence κ_{obs} , the predicted field by our networks κ_{DL} , and the underlying noiseless convergence κ_{true} . Figure 3 compares the lensing fields for a given realization. The predicted convergence κ_{DL} is obtained by the networks trained with 30000 training sets. As seen in the figure, the predicted field has a similar smoothness to the true κ_{true} , and significant errors in the κ_{DL} field. We also find some filamentary structures extending over a few degree lengths that look similar between κ_{DL} and κ_{true} , while more compact structures such as peaks are found to be different. Since such peaks in noiseless convergence are generated by massive galaxy clusters [29], the deep-learning denoising in this paper is probably less effective for searching for the massive objects in the Universe. Nevertheless, the reconstructed convergence by the networks shows a similar level of clumpiness and morphology to the true convergence over arcmin to degree scales. From the comparison, we expect our networks can be good at estimating summary statistics including non-Gaussian information, but they may not work for reconstruction of highly compact and rare features in the image.

B. Reconstruction of summary statistics

We discuss reconstruction of summary statistics. Figure 4 shows the average of one-point PDFs and that of power spectra for the predicted field κ_{DL} over 1000 realizations of input noisy κ_{obs} . In this figure, the red points

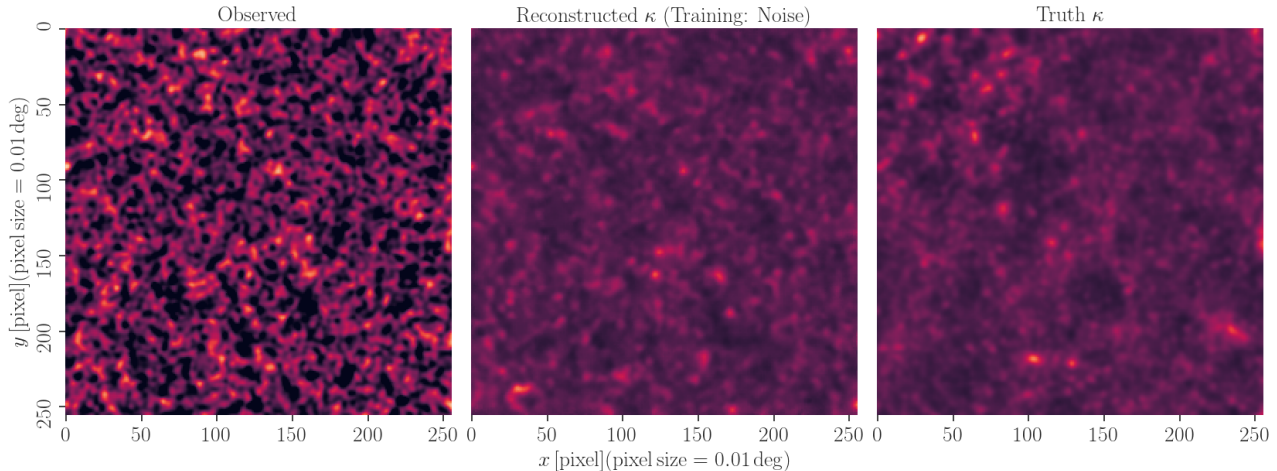


FIG. 3. An example of image-to-image translation by our networks. The left panel shows input noisy convergence map, while the right is for true (noiseless) convergence. The medium represents the reconstructed map by our networks. For the reconstructed map, we first obtain the underlying noise field from the generator in our networks and then derive the convergence map by the residual between the input noisy map and the predicted noise. In this figure, we use the networks trained by 30000 image pairs.

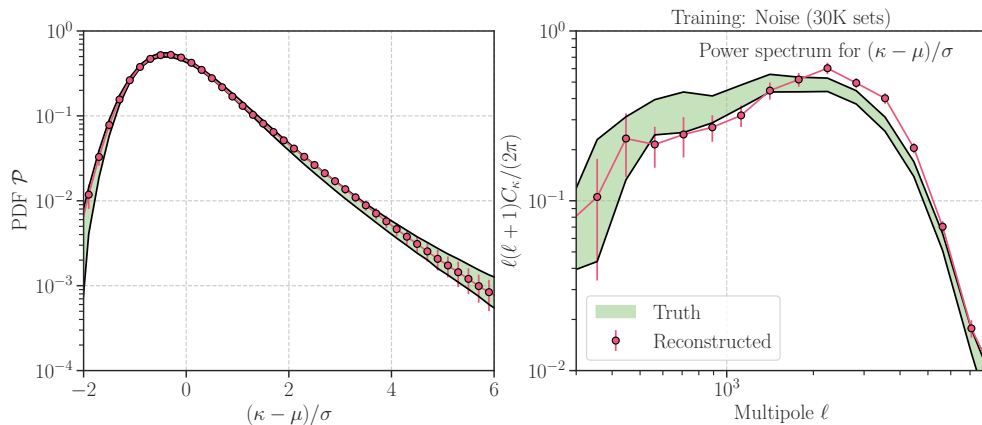


FIG. 4. Comparison of weak-lensing summary statistics. The left panel shows the one-point probability distribution functions, and the right panel compares the power spectra. In each panel, we normalize the convergence so as to have zero mean and unit variance. The red points with error bars represent the summary statistics for the reconstructed field by our deep-learning method (the points and error bars are for the average and the rms over 1000 realizations for testing, respectively), while the green shaded regions show the 1σ variance of the true values. We evaluate the variance by using 1000 noiseless weak lensing maps with a sky coverage of 2.5×2.5 squared degrees.

show the average statistics for κ_{DL} and the error bars represents the standard deviation over 1000 realizations. For comparison, we also show the 1σ variance of statistics as green filled region in the figure. This confidence region is defined by the rms of PDF and power spectrum for true underlying fields κ_{true} over 1000 realizations. Note that the results shown in Figure 4 are obtained by one of our

networks with 30000 training sets (we have 10 networks that are trained with varying the number of training sets based on bootstrap sampling). Figure 4 demonstrates our deep-learning method can reconstruct the shape of one-point PDF of underlying convergence field on average, while the reconstructed power spectrum by our network has a systematic bias.

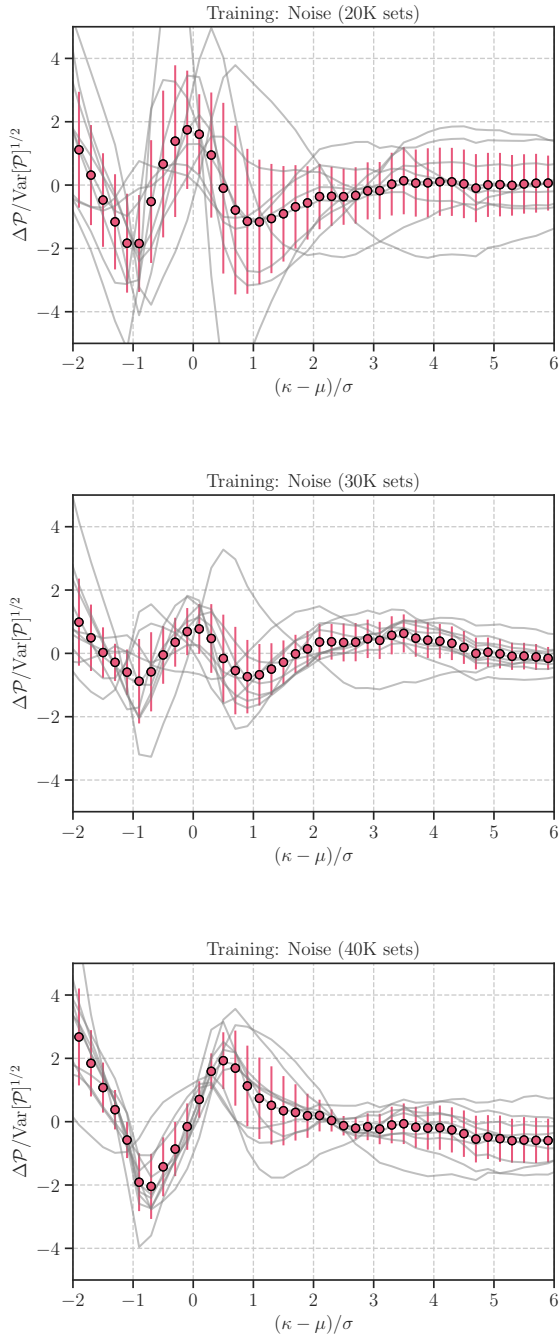


FIG. 5. The dependence of the bias in one-point PDF of the convergence field on the number of training sets. Three different panels show the results by the network based on different numbers of training sets, 20000, 30000, and 40000 image pairs from top to bottom. In each panel, the vertical axis shows the bias in convergence PDF with respect to the true noiseless counterpart and the horizontal axis is the value of convergence (normalized so as to have zero mean and unit variance). The gray lines show the results over 10 bootstrap realizations, while the red points and error bars are the average and standard deviation over 10 realizations. We note that the vertical axis is normalized by the statistical uncertainty of true PDF at each bin assuming a sky coverage of 2.5×2.5 squared degrees. The bootstrap scatter is found to be similar to the statistical uncertainty.

We also examine the variation of the averaged PDF and that of power spectrum over 10 networks with different realizations. Now we define the bias of a given statistic \mathcal{S} at i -th bin as

$$\text{Bias}[\mathcal{S}_i] \equiv \frac{\bar{\mathcal{S}}_i(\kappa_{\text{DL}}) - \bar{\mathcal{S}}_i(\kappa_{\text{true}})}{\text{Var}[\mathcal{S}_i(\kappa_{\text{true}})]^{1/2}}, \quad (17)$$

where \mathcal{S}_i is the statistic at i -th bin, $\bar{\mathcal{S}}_i(\kappa_{\text{DL}})$ is the averaged statistic for the predicted field by our networks, $\bar{\mathcal{S}}_i(\kappa_{\text{true}})$ is the average for underlying noiseless field, and $\text{Var}[\mathcal{S}_i(\kappa_{\text{true}})]$ represents the variance of \mathcal{S}_i for noiseless field.

Figure 5 shows the bias in averaged PDF over 10 different networks. The top, middle and bottom panels in the figure show the bias in PDF based on networks with 20000, 30000, and 40000 training sets, respectively. In each panel, we show the result of 10 networks by bootstrap sampling of training sets. The gray lines show the biases obtained by 10 different networks. The red points and error bars are the average and rms over 10 realizations of network. According to this figure, we find ~ 30000 training sets are sub-optimal to have a less biased estimate of PDF on average. The average bias level in reconstruction of PDF is found to be $\lesssim 1\sigma$ over the wide range of $|(\kappa - \mu)/\sigma| \lesssim 1$. It would be worth noting that our networks will be able to reconstruct the PDF of noiseless lensing convergence at $(\kappa - \mu)/\sigma \sim 0$ where the noise completely dominates in the original noisy map. We also find the training of networks can depend on the realization of input data sets. Even if we set the number of training data sets to be 30000, we find one of 10 networks shows a bias in PDF at $|(\kappa - \mu)/\sigma| \lesssim 1$ with a level of $\sim 2\sigma$. Figure 5 clearly demonstrates that the network will have a variety due to the statistical fluctuations in input data sets. This suggests that training based on single realization of training sets is not sufficient for denoising weak lensing maps.

Figure 6 shows the bias in averaged power spectrum over 10 different networks. Similar to the one-point PDF, we also find a non-negligible scatter over 10 different networks and ~ 40000 realizations will be sub-optimal for an unbiased estimate of power spectrum. Note that the lensing power spectrum can be estimated without denoising procedure and we already have some unbiased estimators of lensing power spectrum in practice [35–37]. Therefore, we expect the biases shown in Figure 6 will not be relevant to actual cosmological analyses. Rather, the figure indicates that our network may not use the Fourier decomposition to separate the noise and underlying lensing fields. To see the reconstruction in Fourier space, we compute the cross correlation between the predicted and true noiseless maps. We find the ratio between the cross power spectrum and the true auto power spectrum to be ~ 0.5 at $\ell = 500$ and ~ 0.1 at $\ell = 5000$. Hence, the denoising with our networks looks less efficient in Fourier space.

We also study the variance in two summary statistics of reconstructed convergence. We find the variance in

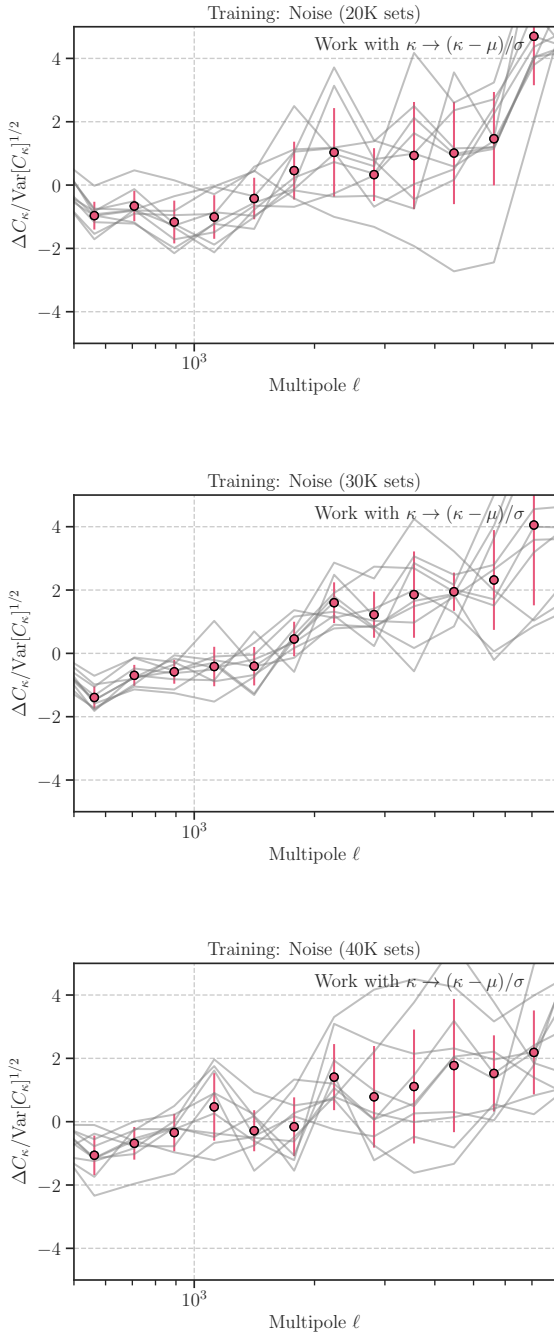


FIG. 6. Similar to Figure 5, but this figure is for the power spectrum.

one-point PDF for reconstructed field is close to that for true noiseless field at $(\kappa - \mu)/\sigma > 3$, but the variance for PDF of κ_{DL} can be smaller by a factor of 0.5 – 0.75 at $(\kappa - \mu)/\sigma \lesssim 3$. Also, the variance in power spectrum for κ_{DL} is found to range from 75 – 100% of the true variance. Hence, the reconstruction uncertainty in summary statistics will mainly arise from a variety of model

parameters in the networks as shown in the error bars in Figures 5 and 6.

C. Reconstruction for individual realizations

Apart from the averaged property, we here consider how our networks can reproduce summary statistics of noiseless lensing convergence on realization-by-realization basis. For this purpose, we introduce the following chi-square quantity:

$$\chi^2(r; \mathcal{S}) = \sum_{i,j} \mathbf{C}_{ij}^{-1} \left[\mathcal{S}_i^{(r)}(\kappa_{\text{DL}}) - \mathcal{S}_i^{(r)}(\kappa_{\text{true}}) \right] \times \left[\mathcal{S}_j^{(r)}(\kappa_{\text{DL}}) - \mathcal{S}_j^{(r)}(\kappa_{\text{true}}) \right], \quad (18)$$

where $\mathcal{S}_i^{(r)}(\kappa_{\text{DL}})$ and $\mathcal{S}_i^{(r)}(\kappa_{\text{true}})$ are the statistics of \mathcal{S} at i -th bin for r -th realization of the predicted field by networks and underlying true noiseless field, respectively. The covariance \mathbf{C} is defined by

$$\bar{\mathcal{D}}_i = \frac{1}{N_r} \sum_r \left[\mathcal{S}_i^{(r)}(\kappa_{\text{DL}}) - \mathcal{S}_i^{(r)}(\kappa_{\text{true}}) \right], \quad (19)$$

$$\mathbf{C}_{ij} = \frac{1}{N_r - 1} \sum_r \left[\mathcal{S}_i^{(r)}(\kappa_{\text{DL}}) - \mathcal{S}_i^{(r)}(\kappa_{\text{true}}) - \bar{\mathcal{D}}_i \right] \times \left[\mathcal{S}_j^{(r)}(\kappa_{\text{DL}}) - \mathcal{S}_j^{(r)}(\kappa_{\text{true}}) - \bar{\mathcal{D}}_j \right], \quad (20)$$

where N_r is the number of realizations of data sets and we set to be $N_r = 1000$. As in Eq. (18), the chi-square quantity can be defined on realization-by-realization basis. When the statistic \mathcal{S} follows a multivariate Gaussian random field and it holds $\bar{\mathcal{D}}_i = 0$, the quantity defined by Eq. (18) should follow a chi-square distribution with N_{bin} degrees of freedom, where N_{bin} is equal to the number of bins. Therefore, the distribution of $\chi^2(r; \mathcal{S})$ is thought to be a good measure of the precision of reconstruction of summary statistics \mathcal{S} with our deep-learning networks. In this subsection, we use the networks based on 30000 training sets.

Figure 7 summarizes the distribution of $\chi^2(r; \mathcal{S})$ for one-point PDF and power spectrum. When calculate the chi-square values, we restrict the range of the variables as $(\kappa - \mu)/\sigma = [-2, 6]$ for PDF and $\ell = [300, 5000]$ for power spectrum. The blue points with error bars shows the distribution of $\chi^2(r; \mathcal{S})$ defined by Eq. (18) from 1000 realizations of κ_{DL} and κ_{true} , while the green histograms represent the chi-square quantity for $\mathcal{S}_i^{(r)}(\kappa_{\text{true}})$. The black line shows the expected χ^2 distribution. The blue error bar represents the standard deviation over 10 bootstrap networks. Compared with the black line and green histograms, we first confirm two summary statistics can be approximated as multivariate Gaussian field. Assuming the bias of summary statistics is zero, i.e. $\bar{\mathcal{D}}_i = 0$, we find the resulting distribution is biased compared to the expected distribution. Among 1000 realizations of the PDF, 169.7 ± 203.54 realizations are found at the

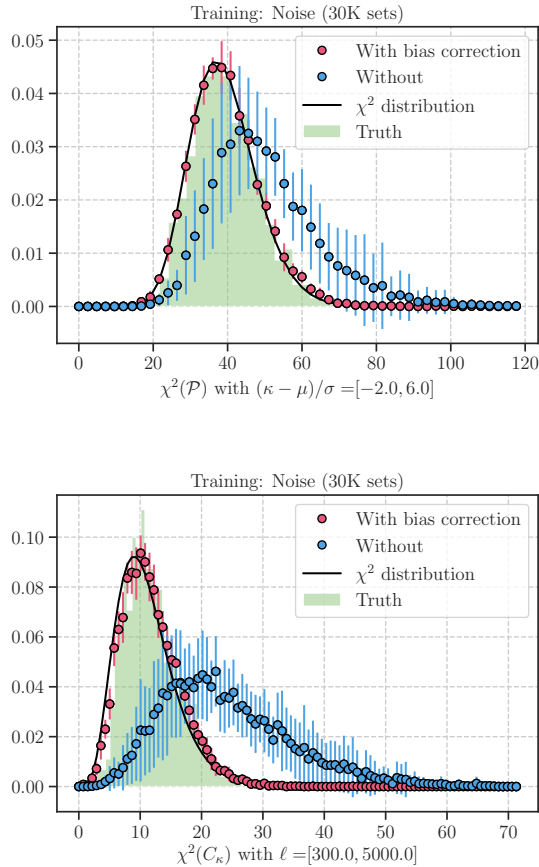


FIG. 7. The distribution of chi-square values of the one-point PDF (top) and power spectrum (bottom). We define the chi-square so that it can follow the chi squared distribution with appropriate degrees of freedom if the summary statistics follow a multivariate Gaussian and if our network can estimate the summary statistics in an unbiased way. In each panel, the black line shows the expected chi square distribution from a Gaussian data set and the green boxes are the distribution obtained from 1000 noiseless convergence maps. The blue points with error bars show the distribution of our chi square quantity (see Eq. 18) and the red points are the results when the bias in the summary statistics through reconstruction is properly included. The blue and red error bars represent the standard deviation over 10 bootstrap realizations in our networks.

outside of 99% confidence level of the expected distribution. For power spectrum, the networks misunderstand 413.1 ± 246.66 realizations to be at the outside of 99% confidence level. According to these experiments, we conclude there is an about 83% chance that our networks reproduce the underlying one-point PDF with 99% confidence level.

When including the bias of $\bar{\mathcal{D}}_i$ in Eq. (18), we find the resulting distribution of chi-square quantity is close to the expected distribution for PDF and power spectrum. The

red points with error bars in Figure 7 are the distribution with bias correction in Eq. (18). The summary statistics predicted by our networks are very similar to the true counterparts in a statistical sense if we can include the bias correction properly.

D. Cosmology dependence of reconstruction bias

As in Section IV C, our networks can make the reconstructed summary statistics consistent with the underlying true ones on a realization-by-realization basis, if the bias in reconstruction is corrected. Since the training of our networks is based on numerical simulations with fixed cosmological model and source redshift distribution, we need to study if the bias in reconstruction can be sensitive to the physical model in training data sets or not.

To study further systematic errors in the bias correction due to imperfect knowledge of the true cosmological model, we use additional 10 realizations of ray-tracing simulations with cosmological models different from our fiducial case [38]. We consider two different cosmological models by varying the amplitude of curvature perturbations A_s with $\pm 10\%$ in logarithmic space. Note that the 10% difference in $\ln A_s$ is significantly large compared to the recent cosmological constraints by the cosmic microwave background experiment [39, 40] and comparable to the latest constraints from the weak lensing two-point correlation [41–43]. These additional simulations are designed so as to cover the same sky coverage of 5×5 squared degrees and source redshift of 1 as our fiducial run. We produce 1000 realizations of noisy convergence from the additional simulations in the same way as in Section III B. We then input the 1000 noisy maps to our networks to see if the resulting bias in reconstruction of summary statistics differs from the results in Figures 5 and 6.

Figure 8 shows the bias in reconstruction when we input noisy convergence maps with different $\ln A_s$. The solid line shows the bias for the maps with higher $\ln A_s$ and dashed line is for lower $\ln A_s$. These lines are the average biases over 10 networks trained with 30000 data sets, while the red points with error bar represent the results for our fiducial model. We find that the 10% uncertainty in $\ln A_s$ will be irrelevant for reconstruction based on our networks. Note that the denoising with our networks is performed on the field of view of 2.5×2.5 squared degrees. Although the statistical property of lensing convergence can change by other parameters as the mean matter density Ω_{m0} and the source redshift distribution, there exists a strong degeneracy among $\ln A_s$, Ω_{m0} and source redshift (e.g. see Ref [4]). Therefore, we argue that our experiments by varying $\ln A_s$ is sufficient to study a possible systematic error in the bias correction for denoising of 2.5×2.5 squared-degree lensing maps. We would need more careful studies to correct the bias in summary statistics for much larger survey areas.

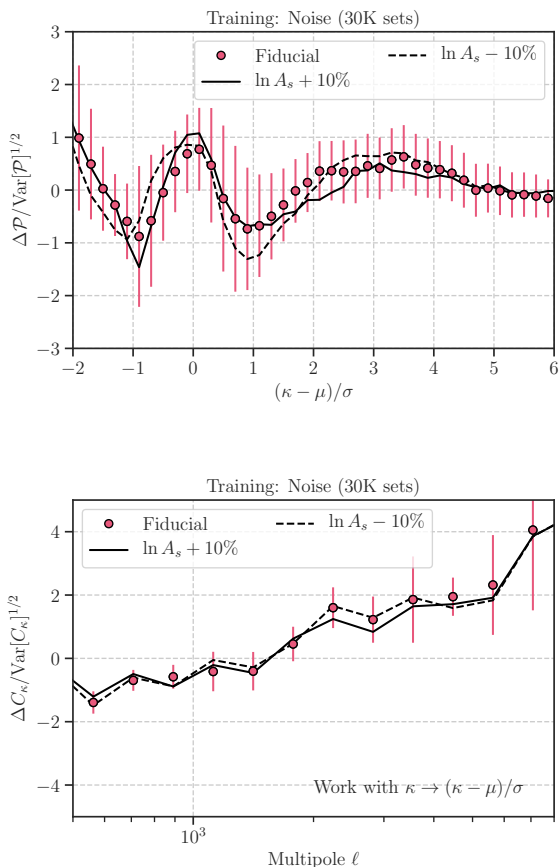


FIG. 8. The bias in estimation of summary statistics due to imperfect knowledge of true convergence map. The top shows the bias in one-point PDF, while the bottom is for power spectrum. The red point shows our fiducial case when the validation data set has been generated from the same cosmological model as training data and error bars are estimated with 10 bootstrap realizations. The solid and dashed lines represent the bias when the input data set follows different cosmological models from the fiducial case.

E. Comparison on pixel-by-pixel basis

So far, we have focused on the statistical properties of weak lensing convergence predicted by our networks. In this subsection, we test and validate our denoising method on a pixel-by-pixel basis. Figure 9 is a simple scatter plot of lensing convergence in $\kappa_{\text{DL}} - \kappa_{\text{true}}$ plane, where κ_{DL} is the reconstructed one and κ_{true} is the noiseless counterpart. For this figure, we show the results from 1000 realizations of κ_{DL} and κ_{true} from single networks trained by 30000 data sets. The dashed line in the figure represents the one-to-one correspondence, while the deeper color shows denser region in the $\kappa_{\text{DL}} - \kappa_{\text{true}}$ plane. The figure shows that the predicted field by our networks follows some probability distribution with the width of $\sim 1\sigma$ for a given κ_{true} , where σ is the rms of κ_{true} in

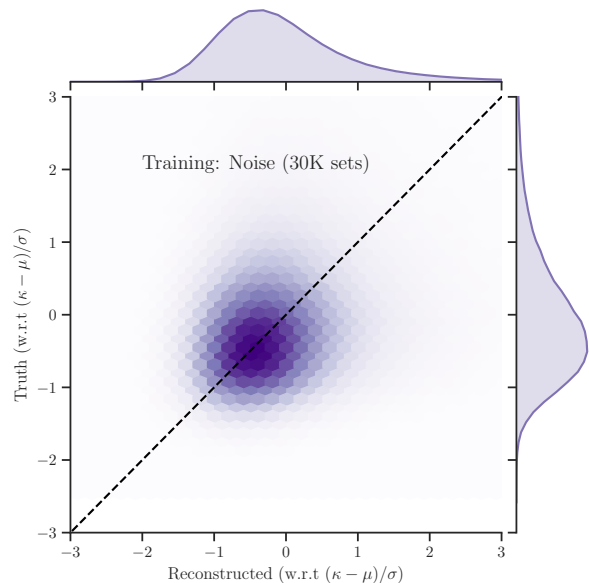


FIG. 9. An example of scatter plot between the reconstructed convergence and true noiseless convergence. The dashed line shows the one-to-one correspondence. In this figure, we use the networks trained by 30000 image pairs and then adopt it to 1000 test data.

a 2.5×2.5 squared-degrees sky, while the width slightly changes as the input value of κ_{true} .

In practice, the relevant statistical quantity of denoising on a pixel-by-pixel basis will be the conditional distribution function of κ_{true} for a given κ_{DL} , referred to as $\text{Prob}(\kappa_{\text{true}}|\kappa_{\text{DL}})$. This probability distribution function can determine the bias in the predicted field compared to the true counterpart at the pixel level (the angular size of 0.6 arcmin). Figure 10 shows the probability distribution of $\text{Prob}(\kappa_{\text{true}} - \kappa_{\text{DL}}|\kappa_{\text{DL}})$ which should have a peak around the origin if the denoising with our networks reproduce κ on a pixel-by-pixel basis. In this figure, we divide the predicted field into three classes by its pixel value $\mathcal{K} = (\kappa_{\text{DL}} - \mu_{\text{DL}})/\sigma_{\text{DL}}$, where μ_{DL} is the mean and σ_{DL} is the rms of the field of κ_{DL} . We define high density regime by the pixel values of $\mathcal{K} > 2$, medium density regime by $0 < \mathcal{K} < 2$, and low density regime by $-2 < \mathcal{K} < 0$.

Figure 10 suggests that our networks return biased estimates for high and medium density regimes with a $\simeq -2\sigma$ and -0.5σ level, respectively. However, our networks can predict the true noiseless field at low density regime on average in an unbiased way. The width of $\text{Prob}(\kappa_{\text{true}} - \kappa_{\text{DL}}|\kappa_{\text{DL}})$ decreases as κ_{DL} becomes smaller. Figure 10 demonstrates that the denoising with our network can open new window to provide a detailed picture of under-dense region in the Universe which has been hidden by the observational noise.

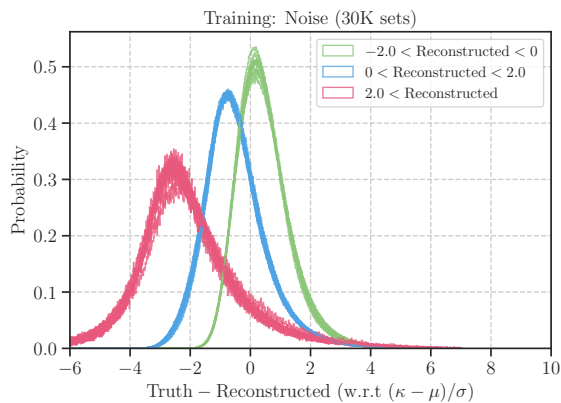


FIG. 10. The conditional probability distribution function of true noiseless convergence for a given range of the reconstructed convergence. The horizontal axis shows the difference between true and reconstructed convergence. Therefore, if we find the peak around zero in the horizontal axis, the network can have an unbiased estimate of convergence on pixel-by-pixel basis on average. The green lines show the probability for the range of reconstructed convergence to be $[-2, 0]$, and the blue and red are for $[0, 2]$ and $[2, \infty]$, respectively. Each colored line shows the result from 10 different bootstrap realizations.

V. FUTURE PROSPECTS IN UPCOMING SURVEY

Upcoming galaxy imaging surveys are aimed at generating accurate lensing maps by increasing the source number density and the area coverage. These include the Wide Field Infrared Survey Telescope (WFIRST⁴), the Large Synoptic Survey Telescope (LSST⁵), and the Euclid satellite⁶

Since the noise rms of weak lensing maps can scale with the inverse of source number density, we expect upcoming surveys with higher source number density can provide less noisy map. We here examine if our denoising method works for such high-precision measurements. As a representative example, we assume the source number density to be 70 arcmin^{-2} , and fix the rms of shape noise for individual galaxies $\sigma_\epsilon = 0.35$ and source redshift $z_{\text{source}} = 1$. In this case, the rms of noisy and noiseless map are found to be 1.4×10^{-2} and 8.6×10^{-3} , respectively. This set up roughly corresponds to the upcoming space-based imaging survey WFIRST [44]. Following the method in Section III B and setting $n_{\text{gal}} = 70 \text{ arcmin}^{-2}$ in Eq. (12), we produce new 60000 and 1000 realizations of input data set for training and testing networks, re-

spectively. We then train the networks with 40000 realizations of these new data sets. We obtain 10 different networks for denoising using 10 bootstrap sampling in total.

Figure 11 summarizes the performance of our networks for denoising. In this figure, left and middle panels show the comparison of two summary statistics, one-point PDF and power spectrum. The red points represent the average statistics over 10 bootstrap realizations and 1000 test data sets, while the error bars are defined as

$$\text{Var}[\mathcal{S}(\kappa_{\text{DL}})]_{\text{stat}} + \text{Var}[\bar{\mathcal{S}}(\kappa_{\text{DL}})]_{\text{bootstrap}}. \quad (21)$$

Here the first term is the standard deviation of statistics \mathcal{S} of reconstructed κ_{DL} over 1000 realizations of test data, and the second term is the scatter in the average $\bar{\mathcal{S}}$ over 10 bootstrap networks. If we increase the source number density, our networks perform well for both of the one point PDF and the power spectrum. We next compare the reconstructed field and the true counterpart on a pixel-by-pixel basis. The right panel in Figure 11 shows the conditional probability distribution as shown in Figure 10. Clearly, under-dense regions can still be reconstructed in an unbiased way on average.

VI. CONCLUSION AND DISCUSSION

We have studied denoising weak lensing maps using the conditional adversarial networks developed in Ref [27]. We have developed a training strategy for the networks to denoise noisy lensing maps. Our findings are summarized as follows. The networks learn efficiently mapping from input noisy maps to the underlying noise field. About 30000 realizations of image pairs are found to be sub-optimal for efficient training of networks to denoise weak lensing with a sky coverage of 2.5×2.5 squared degrees and with a similar noise level to the ongoing ground-base galaxy surveys [32]. The trained networks reproduce the one-point PDF of noiseless weak lensing maps with deviations within a 1σ level. There are $\sim 83\%$ chances that the reconstructed PDF is consistent with the true noiseless counterpart with 99% confidence level. Although the networks do not reproduce the noiseless power spectrum equally well if we assume the noise level in the ongoing survey, we find that the performance can be improved in upcoming survey with higher source number density. When assuming the source number density of 70 arcmin^{-2} , the one-point PDF and power spectrum are in good agreement with the true counterparts. Interestingly, in either case of ongoing or upcoming surveys, our denoising method can provide an unbiased measure for under-dense regions at the pixel level on average, while it induces slightly more biased estimates for higher positive density regions. We thus conclude that our approach is complementary to most existing analyses which commonly focus on the clustering properties and high density regions of weak lensing maps.

⁴ <https://wfirst.gsfc.nasa.gov/>

⁵ <https://www.lsst.org/>

⁶ <https://www.euclid-ec.org/>

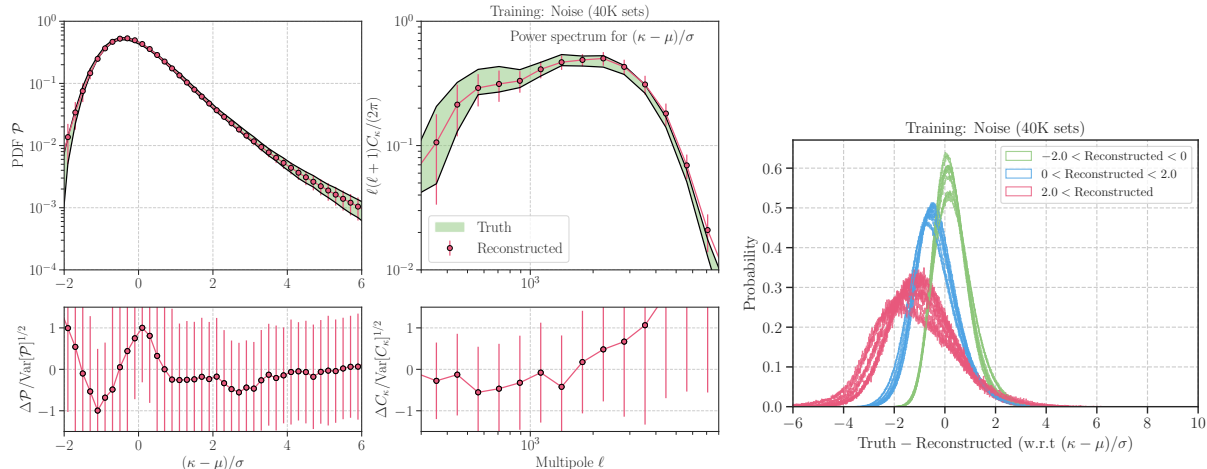


FIG. 11. Forecasts for a hypothetical survey with the high source number density of 70 arcmin^{-2} . *Left and Middle*: Summary statistics similar to Figure 4. The bottom left panels show the average bias in reconstructed PDF normalized to the rms of noiseless PDF, while the bottom middle is for the power spectrum. Note that the red error bars include the statistical error over 1000 test data and the bootstrap scatter over 10 different networks. *Right*: Pixel-by-pixel comparison similar to Figure 10.

Denosing with deep-learning networks can be a powerful tool to probe the cosmic large-scale structure with weak lensing. It is yet to be investigated how the method works for real data sets. In this paper, we have worked with an idealized situation with ignoring several effects in real observations. These include inhomogeneous angular distribution of source galaxies, masking around bright stars, photometric redshift uncertainty, biases in galaxy shape measurement, and the correlation between intrinsic ellipticity and lensing-induced shear (see, Ref [45] and the references therein for systematics in weak lensing measurement). Further studies are necessary to examine the applicability to real data sets. Nevertheless, the denosing with deep learning is a unique method at present to reconstruct the true weak lensing map with an angular resolution of $\sim 1 \text{ arcmin}$. It is worth exploring this approach further for cosmological analyses. In principle, the image-to-image translation with deep learning can be applied for multi-dimensional data sets. Interesting examples in modern cosmology include reconstruction of the three-dimensional matter density field from the observed spatial distribution of galaxies and the component separation in intensity mapping observations over a wide range of frequencies of photons.

It is a challenging task to extract cosmological information in an efficient way from future cosmology surveys. Deep learning is among the promising approaches and is expected to play a crucial role in future statistical analyses. Our method proposed in this paper may be one of the most potent forces that drive big-data analyses in the era of precision cosmology.

ACKNOWLEDGMENTS

The authors thank Akisato Kimura for helpful comments. This work was in part supported by Grant-in-Aid for Scientific Research on Innovative Areas from the MEXT KAKENHI Grant Number (18H04358) and by JST CREST Grant Number JPMJCR1414. Numerical computations presented in this paper were in part carried out on the general-purpose PC farm at Center for Computational Astrophysics, CfCA, of National Astronomical Observatory of Japan.

Appendix A: Training to generate lensing convergence

In this appendix, we study another way of training the network for denosing weak lensing map. We train the networks so that the generator will produce the underlying lensing convergence from an input noisy map. Similar to the method in Section III C, the training is most efficient when noisy data sets consist of 20000 – 40000 independent realizations of noiseless convergence maps combined with 100 noise realizations. After some trials, we find that the summary statistics predicted by the networks do not agree with the true counterparts within a $\sim 3\sigma$ level.

Figure 12 shows the comparison between the predicted convergence by the networks and the true noiseless map. Apparently the networks fail to reproduce the smoothness of convergence with the same level as the truth, and there are too many clumpy structures in the predicted

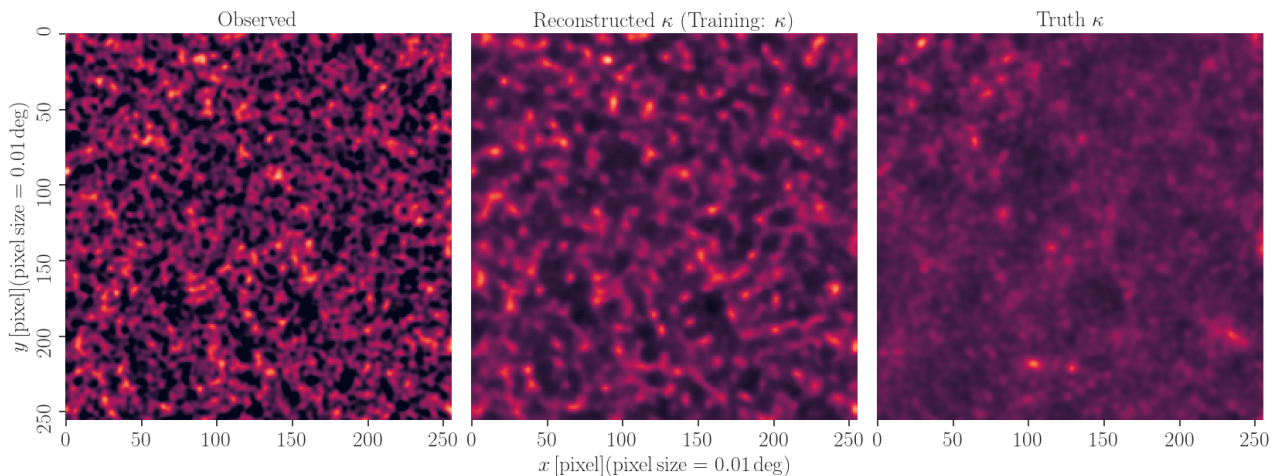


FIG. 12. Similar to Figure 3, but the networks have been trained so that the generator can predict the lensing convergence.

convergence.

-
- [1] M. Bartelmann and P. Schneider, *Phys.Rept.* **340**, 291 (2001), arXiv:astro-ph/9912508 [astro-ph].
- [2] A. Heavens, *Nuclear Physics B Proceedings Supplements* **194**, 76 (2009), arXiv:0911.0350.
- [3] D. Huterer, *General Relativity and Gravitation* **42**, 2177 (2010), arXiv:1001.1758 [astro-ph.CO].
- [4] M. Kilbinger, *Rept. Prog. Phys.* **78**, 086901 (2015), arXiv:1411.0115 [astro-ph.CO].
- [5] B. Jain, U. Seljak, and S. D. M. White, *Astrophys. J.* **530**, 547 (2000), arXiv:astro-ph/9901191 [astro-ph].
- [6] M. J. White and W. Hu, *Astrophys. J.* **537**, 1 (2000), arXiv:astro-ph/9909165 [astro-ph].
- [7] T. Hamana and Y. Mellier, *Mon. Not. Roy. Astron. Soc.* **327**, 169 (2001), arXiv:astro-ph/0101333 [astro-ph].
- [8] T. Matsubara and B. Jain, *Astrophys. J.* **552**, L89 (2001), arXiv:astro-ph/0009402 [astro-ph].
- [9] J. Sato, M. Takada, Y. P. Jing, and T. Futamase, *Astrophys. J.* **551**, L5 (2001), arXiv:astro-ph/0104015 [astro-ph].
- [10] M. Zaldarriaga and R. Scoccimarro, *Astrophys. J.* **584**, 559 (2003), arXiv:astro-ph/0208075 [astro-ph].
- [11] M. Takada and B. Jain, *Astrophys. J.* **583**, L49 (2003), arXiv:astro-ph/0210261 [astro-ph].
- [12] U.-L. Pen, T.-J. Zhang, L. van Waerbeke, Y. Mellier, P.-J. Zhang, and J. Dubinski, *Astrophys. J.* **592**, 664 (2003), arXiv:astro-ph/0302031 [astro-ph].
- [13] M. Jarvis, G. Bernstein, and B. Jain, *Mon. Not. Roy. Astron. Soc.* **352**, 338 (2004), arXiv:astro-ph/0307393 [astro-ph].
- [14] S. Wang, Z. Haiman, and M. May, *Astrophys. J.* **691**, 547 (2009), arXiv:0809.4052 [astro-ph].
- [15] J. P. Dietrich and J. Hartlap, *Mon. Not. Roy. Astron. Soc.* **402**, 1049 (2010), arXiv:0906.3512.
- [16] J. M. Kratochvil, Z. Haiman, and M. May, *Phys. Rev. D* **81**, 043519 (2010), arXiv:0907.0486 [astro-ph.CO].
- [17] J. Schmelzle, A. Lucchi, T. Kacprzak, A. Amara, R. Sgier, A. Rfrgier, and T. Hofmann, (2017), arXiv:1707.05167 [astro-ph.CO].
- [18] A. Gupta, J. M. Z. Matilla, D. Hsu, and Z. Haiman, *Phys. Rev.* **D97**, 103515 (2018), arXiv:1802.01212 [astro-ph.CO].
- [19] D. Ribli, B. . Pataki, and I. Csabai, (2018), arXiv:1806.05995 [astro-ph.CO].
- [20] R. Mandelbaum *et al.*, *Astrophys. J. Suppl.* **212**, 5 (2014), arXiv:1308.4982 [astro-ph.CO].
- [21] M. Bartelmann, R. Narayan, S. Seitz, and P. Schneider, *Astrophys. J.* **464**, L115 (1996), arXiv:astro-ph/9601011 [astro-ph].
- [22] S. L. Bridle, M. P. Hobson, A. N. Lasenby, and R. Saunders, *Mon. Not. Roy. Astron. Soc.* **299**, 895 (1998), arXiv:astro-ph/9802159 [astro-ph].
- [23] P. J. Marshall, M. P. Hobson, S. F. Gull, and S. L. Bridle, *Mon. Not. Roy. Astron. Soc.* **335**, 1037 (2002), arXiv:astro-ph/0112396 [astro-ph].
- [24] J.-L. Starck, S. Pires, and A. Refregier, *Astron. Astrophys.* **451**, 1139 (2006), arXiv:astro-ph/0503373 [astro-ph].
- [25] E. Deriaz, J.-L. Starck, and S. Pires, *A&A* **540**, A34 (2012), arXiv:1201.5214.
- [26] N. Jeffrey *et al.* (DES), *Mon. Not. Roy. Astron. Soc.* **479**, 2871 (2018), arXiv:1801.08945 [astro-ph.CO].
- [27] P. Isola, J.-Y. Zhu, T. Zhou, and A. A. Efros, *ArXiv e-prints* (2016), arXiv:1611.07004 [cs.CV].
- [28] P. Schneider, *Mon. Not. Roy. Astron. Soc.* **283**, 837 (1996), arXiv:astro-ph/9601039 [astro-ph].
- [29] T. Hamana, M. Takada, and N. Yoshida, *Mon. Not. Roy.*

- Astron. Soc. **350**, 893 (2004), arXiv:astro-ph/0310607 [astro-ph].
- [30] O. Ronneberger, P. Fischer, and T. Brox, ArXiv e-prints (2015), arXiv:1505.04597 [cs.CV].
- [31] M. Sato, T. Hamana, R. Takahashi, M. Takada, N. Yoshida, T. Matsubara, and N. Sugiyama, *Astrophys. J.* **701**, 945 (2009), arXiv:0906.2237 [astro-ph.CO].
- [32] R. Mandelbaum *et al.*, *Publ. Astron. Soc. Japan* (2017), 10.1093/pasj/psx130, arXiv:1705.06745 [astro-ph.CO].
- [33] I. J. Goodfellow, J. Pouget-Abadie, M. Mirza, B. Xu, D. Warde-Farley, S. Ozair, A. Courville, and Y. Bengio, ArXiv e-prints (2014), arXiv:1406.2661 [stat.ML].
- [34] D. P. Kingma and J. Ba, ArXiv e-prints (2014), arXiv:1412.6980.
- [35] W. Hu and M. J. White, *Astrophys. J.* **554**, 67 (2001), arXiv:astro-ph/0010352 [astro-ph].
- [36] C. Hikage, M. Takada, T. Hamana, and D. Spergel, *Mon. Not. Roy. Astron. Soc.* **412**, 65 (2011), arXiv:1004.3542 [astro-ph.CO].
- [37] M. R. Becker and E. Rozo, *Mon. Not. Roy. Astron. Soc.* **457**, 304 (2016), arXiv:1412.3851.
- [38] H.-J. Seo, M. Sato, M. Takada, and S. Dodelson, *ApJ* **748**, 57 (2012), arXiv:1109.5639.
- [39] P. A. R. Ade *et al.* (Planck), *Astron. Astrophys.* **594**, A13 (2016), arXiv:1502.01589 [astro-ph.CO].
- [40] N. Aghanim *et al.* (Planck), (2018), arXiv:1807.06209 [astro-ph.CO].
- [41] H. Hildebrandt *et al.*, *Mon. Not. Roy. Astron. Soc.* **465**, 1454 (2017), arXiv:1606.05338 [astro-ph.CO].
- [42] M. A. Troxel *et al.* (DES), *Mon. Not. Roy. Astron. Soc.* **479**, 4998 (2018), arXiv:1804.10663 [astro-ph.CO].
- [43] C. Hikage *et al.* (HSC), Submitted to: *Publ. Astron. Soc. Jap.* (2018), arXiv:1809.09148 [astro-ph.CO].
- [44] D. Spergel, N. Gehrels, C. Baltay, D. Bennett, J. Breckinridge, M. Donahue, A. Dressler, B. S. Gaudi, T. Greene, O. Guyon, C. Hirata, J. Kalirai, N. J. Kasdin, B. Macintosh, W. Moos, S. Perlmutter, M. Postman, B. Rauscher, J. Rhodes, Y. Wang, D. Weinberg, D. Benford, M. Hudson, W.-S. Jeong, Y. Mellier, W. Traub, T. Yamada, P. Capak, J. Colbert, D. Masters, M. Penny, D. Savransky, D. Stern, N. Zimmerman, R. Barry, L. Bartusek, K. Carpenter, E. Cheng, D. Content, F. Dekens, R. Demers, K. Grady, C. Jackson, G. Kuan, J. Kruk, M. Melton, B. Nemati, B. Parvin, I. Poberezhskiy, C. Peddie, J. Ruffa, J. K. Wallace, A. Whipple, E. Wollack, and F. Zhao, ArXiv e-prints (2015), arXiv:1503.03757 [astro-ph.IM].
- [45] R. Mandelbaum, *Ann. Rev. Astron. Astrophys.* **56**, 393 (2018), arXiv:1710.03235 [astro-ph.CO].